



Cite this: *Mater. Adv.*, 2021,
2, 2642Received 27th January 2021,
Accepted 4th March 2021

DOI: 10.1039/d1ma00072a

rsc.li/materials-advances

Negative thermal expansion triggered anomalous thermal upconversion luminescence behaviors in Er³⁺/Yb³⁺-codoped Y₂Mo₃O₁₂ microparticles for highly sensitive thermometry†

Huocheng Lv, Peng Du, * Laihui Luo  and Weiping Li

For the sake of overcoming the challenges of optical thermometers with high sensitivity, we designed Er³⁺/Yb³⁺-codoped Y₂Mo₃O₁₂ microparticles with thermally enhanced upconversion (UC) emission. Excited at 980 nm, the impact of the Yb³⁺ ion content on the UC emission properties of the prepared samples is studied. It is found that the optimal doping content for Yb³⁺ ions in the Y₂Mo₃O₁₂ host is 13 mol% and the involved UC mechanism pertains to the two-photon excitation process. As the temperature increases from 303 to 583 K, an enhancement in the UC emission intensity is seen triggered by the NTE effect. Furthermore, *via* use of the fluorescence intensity rate, the thermometric behaviors of the Y₂Mo₃O₁₂:Er³⁺/0.22Yb³⁺ microparticles are explored, in which their maximum absolute and relative sensitivities are 6.79% K⁻¹ and 0.79% K⁻¹, respectively. Additionally, in comparison with those of the Y₂Mo₃O₁₂:Er³⁺/0.22Yb³⁺ microparticles, Y₂Mo₃O₁₂:Er³⁺/0.22Yb³⁺@BiOF: Tm³⁺/Yb³⁺ composites exhibit superior thermometric properties with high absolute and relative sensitivities of 16.89% K⁻¹ and 1.09% K⁻¹, respectively. As Y₂Mo₃O₁₂ compounds have NTE properties and high thermal stability, our findings may inspire new insight into developing thermally enhanced upconversion materials for highly sensitive thermometry.

1. Introduction

Upconversion (UC) emission *via* the use of rare-earth ion doped luminescent materials is regarded as a feasible strategy to realize versatile applications in many aspects, such as high-resolution bioimaging, light-emitting diodes, optical thermometry, pollutant degradation, *etc.*^{1–5} In particular, the utilization of UC emission to implement optical thermometry has attracted considerable attention owing to its satisfactory features (*e.g.*, rapid response, high spatial resolution, non-contact readout, *etc.*) in comparison with these of traditional thermometers.^{6,7} Currently, the fluorescence intensity rate (FIR), which makes use of the temperature-dependent emission intensities of thermally coupled levels (TCLs) of rare-earth ions, has been greatly researched for optical thermometry.^{8,9} In terms of the TCLs, their energy band gap (ΔE) should be within a certain range of 200–2000 cm⁻¹, which is not of benefit for achieving high relative sensitivity (*i.e.*, $S_r \propto \Delta E/kT^2$).^{10,11} Thus, a new technique,

which takes advantage of the temperature-dependent FIR value of two emitting centers, was proposed to circumvent this issue. Since the emission of Er³⁺ and Nd³⁺ ions exhibited different temperature dependence, Dong *et al.* found that the absolute sensitivity (*i.e.*, S_a) of NaYF₄:Er³⁺/Nd³⁺/Yb³⁺ UC nanocrystals was 8.9% K⁻¹ and it was higher than that of reported optical thermometers based on TCLs.¹² Also, utilizing the temperature-dependent emission of Er³⁺ and Tm³⁺ ions, Xu *et al.* reported that the maximum S_r value of Y₂O₃:Er³⁺/Tm³⁺/Yb³⁺ nanoparticles was 1.12% K⁻¹.¹³ In spite of these achievements, the implementation of optical thermometry by using UC emission is still hindered by some inherent limitations of upconversion materials, such as weak and impressionable emission. For example, thermal quenching (*i.e.*, loss of the emission at elevated temperature) generally exists in upconversion materials, which greatly restricts the feasibility of UC emission. Consequently, some facile and available strategies should be proposed to figure out this shortage.

Recently, the interest in negative thermal expansion (NTE) materials, whose unit cell volumes decrease as the temperature increases, is increasing owing to their scientific curiosity (*e.g.*, the mechanism behind the NTE) and practical applications (*e.g.*, adjusting the thermal expansion coefficient).^{14,15} Among NTE compounds, A₂Mo₃O₁₂ (A represents a trivalent cation) has

Department of Microelectronic Science and Engineering, School of Physical Science and Technology, Ningbo University, 315211 Ningbo, Zhejiang, China.

E-mail: dp2007good@sina.com, dupeng@nbu.edu.cn

† Electronic supplementary information (ESI) available. See DOI: 10.1039/d1ma00072a



received extensive attention on account of its merits of large chemical flexibility, stable structure, high ion conduction and strong NTE performance.^{16,17} Especially, $\text{Y}_2\text{Mo}_3\text{O}_{12}$ shows the best NTE behaviors with lowest anisotropy since the Y^{3+} ions possess a relatively bigger ionic radius and smaller electronegativity in comparison with other trivalent cations,^{18,19} and thus it has been widely researched as a host material. Interestingly, Wang *et al.* revealed that the NTE effect in $\text{Yb}_2\text{W}_3\text{O}_{12}$ and $\text{Sc}_2\text{Mo}_3\text{O}_{12}$ compounds was of benefit for thermally enhancing the UC emission of rare-earth ions (*i.e.*, Er^{3+} , Ho^{3+} , and Tm^{3+}) due to the lattice distortion and contraction.^{20,21} These results provide an idea that thermally enhanced UC emission is expected to be realized in rare-earth ion doped NTE materials. Nevertheless, the investigation on the thermal enhancement of UC emission as well as its corresponding mechanism in rare-earth ion doped NTE compounds is still not sufficient.

Inspired by this, we selected the Er^{3+} ion as the activator because of its intense green emission originating from the TCLs of $^2\text{H}_{11/2}$ and $^4\text{S}_{3/2}$, whereas the Yb^{3+} ion was employed as the sensitizer since it can capture near-infrared light efficiently and transfer the energy to Er^{3+} ions.^{22,23} With the aid of sol-gel reaction technology, a series of $\text{Er}^{3+}/\text{Yb}^{3+}$ -codoped $\text{Y}_2\text{Mo}_3\text{O}_{12}$ upconverting microparticles were synthesized. The phase structure, morphology and UC emission features of the developed compounds were studied in detail. Furthermore, the NTE effect triggered thermal enhancement of UC emission in the resultant samples was also explored. *Via* the utilization of the FIR technique to analyze the temperature-dependent emission intensities of TCLs, the thermometric properties of the synthesized microparticles in the temperature range of 303–583 K were investigated. Ultimately, to further improve the temperature sensing capacity of the developed microparticles with NTE behaviors, we constructed a composite in which the negative (*i.e.*, $\text{Y}_2\text{Mo}_3\text{O}_{12}:\text{Er}^{3+}/0.22\text{Yb}^{3+}$) and positive (*i.e.*, $\text{BiOF}:\text{Tm}^{3+}/\text{Yb}^{3+}$) thermal expansion materials were involved.

2. Experimental

2.1 Synthesis of $\text{Er}^{3+}/\text{Yb}^{3+}$ -codoped $\text{Y}_2\text{Mo}_3\text{O}_{12}$ microparticles

The sol-gel reaction technique was applied to prepare the $\text{Y}_{2(1-0.01-x)}\text{Mo}_3\text{O}_{12}:0.02\text{Er}^{3+}/2x\text{Yb}^{3+}$ (abbreviated as $\text{Y}_2\text{Mo}_3\text{O}_{12}:\text{Er}^{3+}/2x\text{Yb}^{3+}$; $0 \leq x \leq 0.16$) compounds. Notably, the x value stands for the molar ratio. High purity powders including $(\text{NH}_4)_6\text{Mo}_7\text{O}_{24}\cdot 4\text{H}_2\text{O}$, $\text{Er}(\text{NO}_3)_3\cdot 5\text{H}_2\text{O}$, $\text{Y}(\text{NO}_3)_3\cdot 6\text{H}_2\text{O}$, $\text{Yb}(\text{NO}_3)_3\cdot 5\text{H}_2\text{O}$ and citric acid were used as starting materials. Briefly, $\text{Y}(\text{NO}_3)_3\cdot 6\text{H}_2\text{O}$ ((1.98 – 2 x) mmol), $\text{Er}(\text{NO}_3)_3\cdot 5\text{H}_2\text{O}$ (0.02 mmol), $\text{Yb}(\text{NO}_3)_3\cdot 5\text{H}_2\text{O}$ (2 x mmol) and $(\text{NH}_4)_6\text{Mo}_7\text{O}_{24}\cdot 4\text{H}_2\text{O}$ (0.143 mmol) were weighed and put into a beaker which contained 200 mL of deionized water. Then, 10 mmol of citric acid was added into the above solution under strong mechanical stirring. After that, the beaker was sealed and the temperature was boosted to 80 °C. After stirring for 30 min, the lid was shifted and it was heated at 80 °C for 12 h to remove the water, leading to the generation of a wet-gel. Afterwards, we transferred it to an oven and kept it at 120 °C for another 12 h to form the xerogel. Lastly, the xerogel was sintered at 800 °C for 6 h in a furnace to form the final products.

2.2 Synthesis of $\text{Y}_2\text{Mo}_3\text{O}_{12}:\text{Er}^{3+}/0.22\text{Yb}^{3+}@\text{BiOF}:\text{Tm}^{3+}/\text{Yb}^{3+}$ composites

The $\text{Bi}_{0.94}\text{OF}:0.01\text{Tm}^{3+}/0.05\text{Yb}^{3+}$ ($\text{BiOF}:\text{Tm}^{3+}/\text{Yb}^{3+}$) positive thermal expansion phosphors were prepared by a solid-state reaction method. Powders including Bi_2O_3 , NH_4F , Er_2O_3 and Yb_2O_3 were employed as the raw materials. Proper amounts of these above powders were weighed and mixed adequately by means of an agate mortar. Then, this mixture was kept in a crucible and sintered at 500 °C for 3 h to achieve the $\text{BiOF}:\text{Tm}^{3+}/\text{Yb}^{3+}$ phosphors. After that, a typical self-assembly method was adopted to prepare the $\text{Y}_2\text{Mo}_3\text{O}_{12}:\text{Er}^{3+}/0.22\text{Yb}^{3+}@\text{BiOF}:\text{Tm}^{3+}/\text{Yb}^{3+}$ composites. In brief, proper amounts of $\text{BiOF}:\text{Tm}^{3+}/\text{Yb}^{3+}$ and $\text{Y}_2\text{Mo}_3\text{O}_{12}:\text{Er}^{3+}/0.22\text{Yb}^{3+}$ microparticles (*i.e.*, mass ratio = 1 : 5) were weighed and added into ethanol (30 mL). After stirring for 2 h, the mixture was heated at 80 °C to remove the ethanol, leading to the formation of the $\text{Y}_2\text{Mo}_3\text{O}_{12}:\text{Er}^{3+}/0.22\text{Yb}^{3+}@\text{BiOF}:\text{Tm}^{3+}/\text{Yb}^{3+}$ composites.

2.3 Sample characterization

The crystal structure and crystallinity of the final products were checked using an X-ray diffractometer (Bruker D8 Advance; Cu $K\alpha$ radiation). The elemental composition and morphology of the samples were measured *via* a field-emission scanning electron microscope (FE-SEM; HITACHI SU3500) equipped with an energy-dispersive X-ray spectroscopy (EDS) accessory. The surface properties and thermal stability of the resultant microparticles were examined by using a Fourier transform infrared (FT-IR) spectrophotometer (Bruker Tensor 27) and differential scanning calorimetry and thermogravimetric analysis (DSC-TG) device (SDTQ 600), respectively. An ultraviolet-visible (UV-vis) spectrophotometer (Cary 500) was adopted to record the diffuse reflectance spectrum. The UC emission spectra of the studied samples were detected *via* a fluorescence spectrometer (Edinburgh FS5) with a temperature control system (Linkam HFS600E-PB2) attached.

3. Results and discussion

3.1 Phase structure and microstructure behaviors

The impact of the doping content on the phase compositions of the final products is verified by utilizing X-ray diffraction (XRD). Fig. 1(a) shows the XRD profiles of the $\text{Y}_2\text{Mo}_3\text{O}_{12}:\text{Er}^{3+}/2x\text{Yb}^{3+}$ microparticles. As illustrated, when the Yb^{3+} ion content is low (*i.e.*, $x \leq 0.11$), these recorded diffraction peaks are able to be primarily indexed by the standard orthorhombic $\text{Y}_2\text{Mo}_3\text{O}_{12}$ (JCPDS #28-1541), revealing that the designed $\text{Er}^{3+}/\text{Yb}^{3+}$ -codoped $\text{Y}_2\text{Mo}_3\text{O}_{12}$ compounds are successfully synthesized by means of the sol-gel reaction technique. Nevertheless, two tiny peaks from the impurity phase of $\text{Y}_2\text{Mo}_4\text{O}_{15}$ (JCPDS #53-0358) are detected in the XRD profiles when the doping content is over 11 mol% (*i.e.*, $x = 0.11$), as shown in Fig. 1(a), suggesting that the Yb^{3+} ions present a solubility limitation in the selected host lattices. In order to understand the crystal structure of the studied samples in depth, the Rietveld XRD refinements of the $\text{Y}_2\text{Mo}_3\text{O}_{12}:\text{Er}^{3+}$ and $\text{Y}_2\text{Mo}_3\text{O}_{12}:\text{Er}^{3+}/0.22\text{Yb}^{3+}$ microparticles are



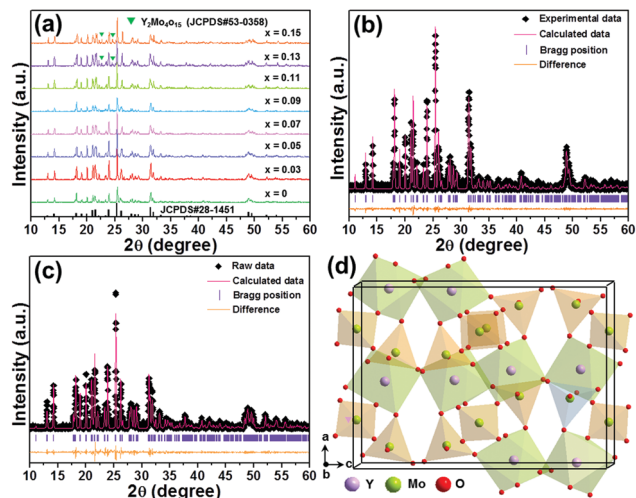


Fig. 1 (a) XRD patterns of the $\text{Y}_2\text{Mo}_3\text{O}_{12}:\text{Er}^{3+}/2x\text{Yb}^{3+}$ microparticles. Rietveld XRD refinement patterns of the (b) $\text{Y}_2\text{Mo}_3\text{O}_{12}:\text{Er}^{3+}$ and (c) $\text{Y}_2\text{Mo}_3\text{O}_{12}:\text{Er}^{3+}/0.22\text{Yb}^{3+}$ microparticles. (d) Crystal structure of the $\text{Y}_2\text{Mo}_3\text{O}_{12}$ unit cell.

performed and the corresponding results are depicted in Fig. 1(b and c), respectively. The refinement results imply that the prepared samples have a pure orthorhombic phase with the $Pbcn$ space group. Furthermore, the lattice constants of the $\text{Y}_2\text{Mo}_3\text{O}_{12}:\text{Er}^{3+}/x\text{Yb}^{3+}$ ($x = 0$ and 0.11) microparticles are demonstrated to be smaller, which are assigned to the different ionic radii between the Y^{3+} ions and dopants (*i.e.*, Er^{3+} , Yb^{3+}), than those of $\text{Y}_2\text{Mo}_3\text{O}_{12}$ (see Table S1, ESI[†]), further confirming the formation of the $\text{Er}^{3+}/\text{Yb}^{3+}$ -codoped $\text{Y}_2\text{Mo}_3\text{O}_{12}$ compounds. Additionally, the Raman spectra also prove the generation of orthorhombic $\text{Y}_2\text{Mo}_3\text{O}_{12}$, as presented in Fig. S1 (ESI[†]). The spatial structure of the $\text{Y}_2\text{Mo}_3\text{O}_{12}$ unit cell is drawn and shown in Fig. 1(d). Evidently, $\text{Y}_2\text{Mo}_3\text{O}_{12}$ with an orthorhombic phase consists of corner-shared MoO_4 tetrahedrons and YO_6 octahedrons, namely, each YO_6 octahedron shares its corner with six MoO_4 tetrahedrons, while each MoO_4 tetrahedron shares its corner with four YO_6 octahedrons. Note that this kind of structure is easily rotated at high temperature, leading to the shrinkage of the crystal lattice as well as promoted energy transfer (ET) between the sensitizer and activator.^{20,21}

To shed more light on the stability of the studied samples, the thermogravimetric (TG) spectrum of the $\text{Y}_2\text{Mo}_3\text{O}_{12}:\text{Er}^{3+}/0.22\text{Yb}^{3+}$ microparticles is illustrated in Fig. S2 (ESI[†]). With elevating the temperature from 300 to 867 K, no significant change is seen in the mass, revealing the excellent thermal stability of the resultant microparticles. The surface performance of the synthesized microparticles is explored by employing the FT-IR spectra, as demonstrated in Fig. S3 (ESI[†]). Furthermore, the FE-SEM images of the final products reveal the non-uniform morphology of the particles with micron sizes (see Fig. S4, ESI[†]), in which the shape and size of the particles are insensitive to the doping concentration. Additionally, the compositional analysis based on the EDS spectrum clarifies the existence of Y, Mo, O, Er and Yb in the studied compounds, as shown in Fig. S5(a) (ESI[†]). Moreover, these elements

(*i.e.*, Y, Mo, O, Er, and Yb) are distributed equally throughout the whole microparticles (see Fig. S5(b-g), ESI[†]). The diffuse reflectance spectra data not only prove the existence of Er^{3+} and Yb^{3+} ions in the studied samples, but also reveal that the energy band gap of the final products is independent of the doping concentration, as depicted in Fig. S6 (ESI[†]).

3.2 UC emission performance of the resultant microparticles

To find the optimal doping content of Yb^{3+} ions in the $\text{Y}_2\text{Mo}_3\text{O}_{12}$ host lattices, the UC emission spectra of the $\text{Y}_2\text{Mo}_3\text{O}_{12}:\text{Er}^{3+}/2x\text{Yb}^{3+}$ microparticles excited at 980 nm were examined and are presented in Fig. 2(a). Clearly, three emission bands with central wavelengths of about 530 nm (*i.e.*, ${}^2\text{H}_{11/2} \rightarrow {}^4\text{I}_{15/2}$), 553 nm (*i.e.*, ${}^4\text{S}_{3/2} \rightarrow {}^4\text{I}_{15/2}$) and 661 nm (*i.e.*, ${}^4\text{F}_{9/2} \rightarrow {}^4\text{I}_{15/2}$) arising from the Er^{3+} ions are observed in the luminescence profiles and their shapes are independent of the doping content except for their intensities.^{24,25} It is revealed in Fig. 2(b) that both the green and red UC emission intensities are reinforced with the increase of the dopant content and arrive at their maximum values when the Yb^{3+} ion concentration is 13 mol% (*i.e.*, $x = 0.13$), whereas the UC emission intensities start to decline with further elevating the doping concentration due to the energy back transfer from Er^{3+} to Yb^{3+} ions. Notably, from the XRD results, one knows that the developed microparticles doped with 13 mol% Yb^{3+} ions exhibit an impurity phase (see Fig. 1(a)). Thus, to eliminate the influence of the impurity phase on the UC emission and thermometric properties of the studied samples, we selected the $\text{Y}_2\text{Mo}_3\text{O}_{12}:\text{Er}^{3+}/0.22\text{Yb}^{3+}$ microparticles as a representative sample since they not only possess a pure phase structure but also show a relatively intense UC emission intensity. The Commission International de l'Eclairage (CIE) coordinates of the $\text{Y}_2\text{Mo}_3\text{O}_{12}:\text{Er}^{3+}/0.22\text{Yb}^{3+}$ microparticles are (0.274, 0.705),

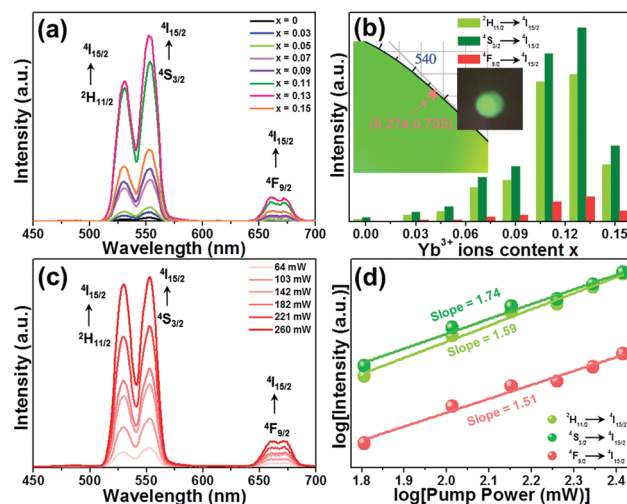


Fig. 2 (a) UC emission spectra of the $\text{Y}_2\text{Mo}_3\text{O}_{12}:\text{Er}^{3+}/2x\text{Yb}^{3+}$ microparticles. (b) Dependence of the emission intensity on doping concentration. The inset shows the CIE coordinate diagram of the $\text{Y}_2\text{Mo}_3\text{O}_{12}:\text{Er}^{3+}/0.22\text{Yb}^{3+}$ microparticles along with their optical image excited at 980 nm. (c) UC emission spectra of the $\text{Y}_2\text{Mo}_3\text{O}_{12}:\text{Er}^{3+}/0.22\text{Yb}^{3+}$ microparticles as a function of pump power. (d) Double logarithmic plots of pump power vs. emission intensities.



which are situated in the green region, and it can emit bright green emission upon 980 nm irradiation (see the inset of Fig. 2(b)). In an attempt to expose the NIR-light-induced UC emission mechanism, the pump power dependent UC emission spectra of the $\text{Y}_2\text{Mo}_3\text{O}_{12}:\text{Er}^{3+}/0.22\text{Yb}^{3+}$ microparticles were recorded and are depicted in Fig. 2(c). As revealed, with raising the pump power, a monotonous increment is seen in the emission intensity without altering the luminescence profiles. As proposed in previous literature,^{24,26} the amounts of photons (*i.e.*, n) which are needed to populate the high excited levels are able to be estimated by using the function of $I_{\text{UC}} \propto P^n$ (herein, I_{UC} and P denote the emission intensity and pump power, respectively). It is evident that the n values of the emission corresponding to the ${}^2\text{H}_{11/2} \rightarrow {}^4\text{I}_{15/2}$, ${}^4\text{S}_{3/2} \rightarrow {}^4\text{I}_{15/2}$ and ${}^4\text{F}_{9/2} \rightarrow {}^4\text{I}_{15/2}$ transitions are 1.74, 1.59 and 1.51 (see Fig. 2(d)), respectively, implying that the above UC emission mechanism is contributed by a two-photon excitation process. Ultimately, the simplified energy level diagram of Er^{3+} and Yb^{3+} as well as the possible luminescence processes is illustrated in Fig. S7 (ESI[†]).

For the sake of exploring the impact of NTE on the UC emission properties of the final products, the evolution of the luminescence profile as a function of temperature in the 303–583 K range is investigated. When excited at 980 nm, the resultant microparticles emit the featured emission of Er^{3+} ions and the positions are hardly impacted by the temperature, whereas the emission intensities are changed with altering the temperature (Fig. 3(a)). As the temperature is increased from 303 to 583 K, the intensities of all the emission bands are appreciably reinforced, as displayed in Fig. 3(b). Especially, the intensity of green UC emission at 530 nm is enhanced by around 4.4-fold when the temperature is boosted from 303 to 583 K, while those at 553 and 661 nm are boosted by about 1.4-fold and 2.6-fold, respectively. As confirmed in previous

literature,^{18,27} one knows that the unit cell volume of the $\text{Y}_2\text{Mo}_3\text{O}_{12}$ host lattice is reduced with rising temperature, leading to the decline of the distance between the sensitizer (*i.e.*, Yb^{3+}) and activator (*i.e.*, Er^{3+}). Consequently, the ET from Yb^{3+} to Er^{3+} ions is able to be promoted and more desired excited levels are generated (Fig. 3(c)),^{20,21} resulting in the thermal improvement of the UC emission intensities. Furthermore, the distortion of the host lattices can also contribute to the enhanced UC emission intensity since it can elevate the possibility of the electronic transitions of rare-earth ions.²⁸ Owing to these two processes, anomalous thermal UC luminescence behaviors are achieved in $\text{Er}^{3+}/\text{Yb}^{3+}$ -codoped $\text{Y}_2\text{Mo}_3\text{O}_{12}$ microparticles. Notably, the increment rates of the obtained emission are different, which is mainly caused by the features of the TCLs of Er^{3+} ions. In particular, with elevating the temperature, electrons located in the ${}^4\text{S}_{3/2}$ level can be pumped to the ${}^2\text{H}_{11/2}$ level *via* the thermal activation process. Also, the population of the ${}^4\text{F}_{9/2}$ level from the ${}^4\text{S}_{3/2}$ level can also be impacted by temperature. Thus, the population of the ${}^2\text{H}_{11/2}$, ${}^4\text{S}_{3/2}$ and ${}^4\text{F}_{9/2}$ levels will be different at high temperature, leading to the diverse enhancement rates in their emission intensities. Aside from the promoted UC emission intensity, the color coordinates of the resultant microparticles are also changed from (0.274, 0.705) to (0.228, 0.739) when the temperature is elevated from 303 to 583 K due to the inconsistent responses of the green and red UC emission to temperature, as displayed in Table S2 (ESI[†]). In addition, with rising temperature, the emitted light becomes brighter and brighter, as demonstrated in the inset of Fig. 3(d), straightforwardly illustrating that the UC emission performance of the rare-earth ions in NTE compounds is able to be promoted *via* heating.

3.3 Thermometric behaviors of the prepared microparticles

As is known, the ${}^2\text{H}_{11/2}$ and ${}^4\text{S}_{3/2}$ levels belong to the TCLs of Er^{3+} ions, which makes Er^{3+} ion based luminescent materials promising candidates for optical thermometry. For the purpose of investigating the thermometric properties of Er^{3+} ions in NET compounds, the normalized temperature-dependent green UC emission spectra of the $\text{Y}_2\text{Mo}_3\text{O}_{12}:\text{Er}^{3+}/0.22\text{Yb}^{3+}$ microparticles are shown in Fig. 4(a). Significantly, the intensity of the ${}^2\text{H}_{11/2} \rightarrow {}^4\text{I}_{15/2}$ transition is improved compared with that of the ${}^4\text{S}_{3/2} \rightarrow {}^4\text{I}_{15/2}$ transition when the temperature is increased from 303 to 583 K, resulting in a temperature-dependent FIR value. As disclosed, the FIR value of the emission arising from the ${}^2\text{H}_{11/2} \rightarrow {}^4\text{I}_{15/2}$ to ${}^4\text{S}_{3/2} \rightarrow {}^4\text{I}_{15/2}$ transitions is boosted from 0.71 to 2.45 with adjusting the temperature in the 303–583 K range (see Fig. 4(b)). From previous reports,^{29,30} it is obvious that the FIR value of TCLs shows a good exponential relation with temperature (*i.e.*, T), as defined below:

$$\text{FIR} = \frac{I_{\text{U}}}{I_{\text{L}}} = A \exp(-\Delta E/kT) \quad (1)$$

where I_{U} and I_{L} refer to the intensities of emission originating from the upper and lower TCLs, respectively, A is a coefficient, ΔE is related to the band gap between the TCLs and k denotes the Boltzmann constant. *Via* the use of eqn (1) to fit the

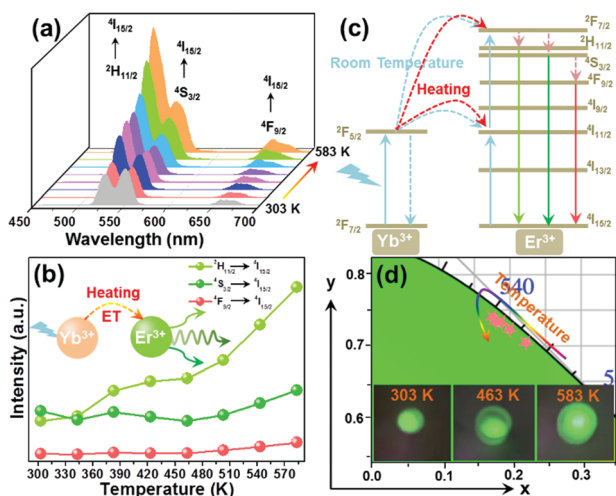


Fig. 3 (a) Temperature-dependent UC emission spectra and (b) emission intensities of the $\text{Y}_2\text{Mo}_3\text{O}_{12}:\text{Er}^{3+}/0.22\text{Yb}^{3+}$ microparticles. (c) Energy level diagram illustrating thermally promoted ET from Yb^{3+} to Er^{3+} ions. (d) CIE coordinate diagram of the $\text{Y}_2\text{Mo}_3\text{O}_{12}:\text{Er}^{3+}/0.22\text{Yb}^{3+}$ microparticles as a function of temperature. The inset shows the optical images of the resultant samples at different temperatures excited at 980 nm.



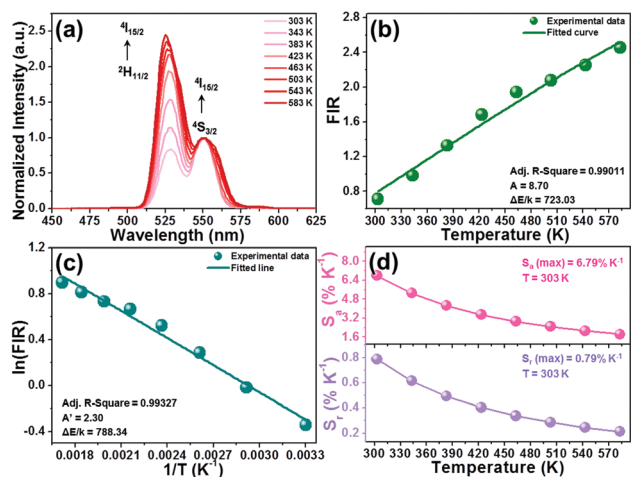


Fig. 4 (a) Normalized green UC emission spectra of the $\text{Y}_2\text{Mo}_3\text{O}_{12}:\text{Er}^{3+}/0.22\text{Yb}^{3+}$ microparticles in the temperature range of 303–583 K. (b) Temperature-dependent FIR value. (c) Plot of $\ln(\text{FIR})$ versus $1/T$ of the $\text{Y}_2\text{Mo}_3\text{O}_{12}:\text{Er}^{3+}/0.22\text{Yb}^{3+}$ microparticles. (d) Dependence of the S_a and S_r values on the temperature.

experimental data, the values of A and $\Delta E/k$ are found to be 8.70 and 723.03, respectively (see Fig. 4(b)). Note that the above function can also be presented in the form of a linear formula:

$$\ln(\text{FIR}) = A' - \Delta E/kT \quad (2)$$

where A' is regarded as a constant. The plot of $\ln(\text{FIR})$ versus $1/T$ is shown in Fig. 4(c). Through linear fitting, one knows that the values of A' and $\Delta E/k$ are 2.30 and 788.34, respectively. Obviously, the $\Delta E/k$ values which are achieved from eqn (1) and (2) present little difference, showing that these fitting results are trustworthy.

To clarify whether the designed materials can be employed as luminescent probes for ratiometric thermometry or not, it is necessary to evaluate their temperature-dependent S_a and S_r , as defined below:^{31,32}

$$S_a = \frac{d\text{FIR}}{dT} = \text{FIR} \times \frac{\Delta E}{kT^2} \quad (3)$$

$$S_r = \frac{1}{\text{FIR}} \frac{d\text{FIR}}{dT} \times 100\% = \frac{\Delta E}{kT^2} \times 100\% \quad (4)$$

Through substituting the fitted values into these functions, the S_a and S_r values of the $\text{Y}_2\text{Mo}_3\text{O}_{12}:\text{Er}^{3+}/0.22\text{Yb}^{3+}$ microparticles as a function of temperature are obtained and shown in Fig. 4(d). It is presented in Fig. 4(d) that both the S_a and S_r values exhibit a monotonous decreasing tendency with the increase of the temperature. Especially, the maximum S_a and S_r values of the $\text{Y}_2\text{Mo}_3\text{O}_{12}:\text{Er}^{3+}/0.22\text{Yb}^{3+}$ microparticles are $6.79\% \text{ K}^{-1}$ and $0.79\% \text{ K}^{-1}$, respectively, which are comparable with previously developed optical thermometers (see Table 1). Considering the thermally enhanced UC emission as well as the relatively high sensitivities, the $\text{Y}_2\text{Mo}_3\text{O}_{12}:\text{Er}^{3+}/2x\text{Yb}^{3+}$ microparticles are promising luminescent probes for optical thermometry.

Table 1 Comparison of the thermometric properties of developed optical thermometers based on rare-earth ion doped luminescent materials

Luminescent materials	Temperature (K)	S_a (K^{-1}) (%)	S_r (K^{-1}) (%)	Ref.
$\text{Bi}_5\text{IO}_7:\text{Er}^{3+}$	303–543	0.69	1.36	4
$\text{BaY}_2\text{O}_4:\text{Er}^{3+}/\text{Yb}^{3+}$	298–573	0.19	—	8
$\beta\text{-NaYF}_4:\text{Yb}^{3+}-\text{Er}^{3+}@\text{SiO}_2$	299–337	—	1.31	30
$\text{Na}_2\text{YMg}(\text{VO}_4)_3:\text{Er}^{3+}/\text{Yb}^{3+}$	303–573	0.77	1.104	31
$\text{NaLuF}_4:\text{Eu}^{3+}@\text{g-C}_3\text{N}_4$	303–503	0.57	0.455	36
$\text{Ca}_8\text{ZnLa}(\text{PO}_4)_7:\text{Tb}^{3+}/\text{Eu}^{3+}$	298–448	—	0.53	38
$\text{Bi}_2\text{SiO}_5:\text{Er}^{3+}/\text{Yb}^{3+}$	298–600	—	0.99	39
$\text{LaNbO}_4:\text{Bi}^{3+}/\text{Eu}^{3+}$	303–483	4.4	1.89	40
$\text{Na}_2\text{YMg}(\text{VO}_4)_3:\text{Er}^{3+},\text{Yb}^{3+}$	303–573	0.77	1.104	41
$\text{Gd}_2\text{O}_3:\text{Er}^{3+}/\text{Yb}^{3+}$	298–578	1.86	1.51	42
$\text{Y}_2\text{Mo}_3\text{O}_{12}:\text{Er}^{3+}/\text{Yb}^{3+}$	303–583	6.79	0.79	This work
$\text{Y}_2\text{Mo}_3\text{O}_{12}:\text{Er}^{3+}/\text{Yb}^{3+}@\text{BiOF}:\text{Tm}^{3+}/\text{Yb}^{3+}$	303–583	16.89	1.09	This work

Aside from utilizing the temperature-dependent emission intensities of TCLs to realize temperature monitoring, another technique, which is based on luminescent compounds with dual-emitting centers, is also intensively adopted. Moreover, it is widely acknowledged that most compounds pertain to positive thermal expansion materials, in which their unit cell volumes are enlarged at elevated temperature, leading to the thermal quenching effect. Obviously, the UC emission performances of the rare-earth ions in positive and negative thermal expansion materials exhibit inverse responses to temperature. Thus, simultaneously taking advantage of the temperature-dependent UC emission intensities of rare-earth ions in negative and positive thermal expansion combined materials would be a valid route to ameliorate the thermometric properties of luminescent materials. As a proof of this guess, we synthesized $\text{Y}_2\text{Mo}_3\text{O}_{12}:\text{Er}^{3+}/0.22\text{Yb}^{3+}@\text{BiOF}:\text{Tm}^{3+}/\text{Yb}^{3+}$ composites and explored their thermometric behaviors. Herein, $\text{BiOF}:\text{Tm}^{3+}/\text{Yb}^{3+}$ phosphors, which can emit intense UC blue emission at 480 arising from the $^1\text{G}_4 \rightarrow ^3\text{H}_6$ transition of Tm^{3+} ions,³³ belong to positive expansion materials and their UC emission intensity gradually decreases with rising temperature (see Fig. S8, ESI†). Upon 980 nm excitation, the UC emission spectra of the designed $\text{Y}_2\text{Mo}_3\text{O}_{12}:\text{Er}^{3+}/0.22\text{Yb}^{3+}@\text{BiOF}:\text{Tm}^{3+}/\text{Yb}^{3+}$ composites as a function of temperature were examined. It is demonstrated in Fig. 5(a) that the intensities of the blue (*i.e.*, Tm^{3+}) and green (*i.e.*, Er^{3+}) emission are dependent on the temperature. In particular, the intensity of Tm^{3+} ions exhibits a downward trend as the temperature changes from 303 to 583 K, whereas that of the Er^{3+} ions shows an opposite changing tendency, as illustrated in Fig. S9 (ESI†). Furthermore, from the normalized temperature-dependent UC emission spectra (Fig. 5(b)), one obtains that the green emission intensity of Er^{3+} ions is sharply enhanced in comparison with that of Tm^{3+} ions, leading to temperature-dependent FIR values. As disclosed in Fig. 5(c), the FIR value of the blue (*i.e.*, Tm^{3+}) to green (*i.e.*, Er^{3+}) emission is greatly increased from 2.17 to 16.93 when the temperature is tuned in the 303–583 K range. Notably, the relationship between the temperature and the FIR value of non-TCLs of rare-earth ions is able to be described as follows:^{34,35}



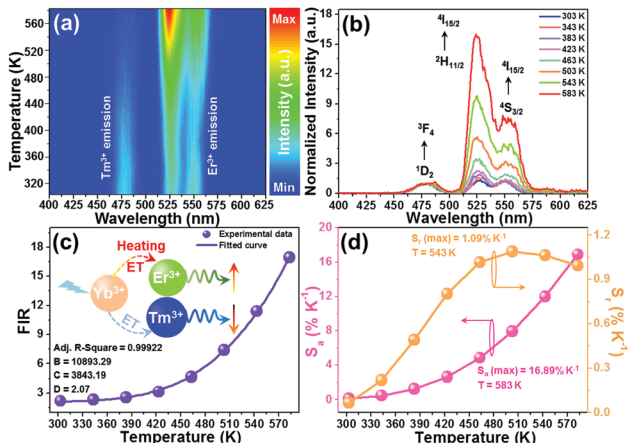


Fig. 5 (a) Contour lines of the $\text{Y}_2\text{Mo}_3\text{O}_{12}:\text{Er}^{3+}/0.22\text{Yb}^{3+}@\text{BiOF}:\text{Tm}^{3+}/\text{Yb}^{3+}$ (*i.e.*, mass rate = 1 : 5) composites as a function of temperature excited at 980 nm. (b) Temperature-dependent UC emission spectra (normalized at 480 nm) and (c) FIR value of the $\text{Y}_2\text{Mo}_3\text{O}_{12}:\text{Er}^{3+}/0.22\text{Yb}^{3+}@\text{BiOF}:\text{Tm}^{3+}/\text{Yb}^{3+}$ composites. (d) Dependence of the S_a and S_r values on the temperature.

$$\text{FIR} = B \exp(-C/T) + D \quad (5)$$

The parameters of B , C and D are all regarded as coefficients. *Via* use of eqn (5), the experimental data are fitted and the values of B , C and D are proved to be 10893.29, 3843.19 and 2.07, respectively (see Fig. 5(c)).

To get deeper insight into the temperature sensing capacity of the developed composite, we explored its temperature-dependent S_a and S_r values by means of the following functions:^{36,37}

$$S_a = \frac{d\text{FIR}}{dT} = B \exp(-C/T) \times (C/T^2) \quad (6)$$

$$S_r = \frac{1}{\text{FIR}} \frac{d\text{FIR}}{dT} \times 100\% = \frac{B \exp(-C/T)}{B \exp(-C/T) + D} \times \frac{C}{T^2} \times 100\% \quad (7)$$

Through substituting the fitted values into these expressions, the temperature-dependent S_a and S_r values of the $\text{Y}_2\text{Mo}_3\text{O}_{12}:\text{Er}^{3+}/0.22\text{Yb}^{3+}@\text{BiOF}:\text{Tm}^{3+}/\text{Yb}^{3+}$ composites are achieved and shown in Fig. 5(d). As the temperature changes in the range of 303–583 K, the S_a value increases rapidly and arrives at its maximum value of 16.89% K^{-1} at 583 K. Similarly, the S_r value is also dependent on the temperature and its maximum value is around 1.09% K^{-1} at 503 K (see Fig. 5(d)). Apparently, in comparison to those of $\text{Y}_2\text{Mo}_3\text{O}_{12}:\text{Er}^{3+}/0.22\text{Yb}^{3+}$ microparticles based on TCLs, the S_a and S_r values of the $\text{Y}_2\text{Mo}_3\text{O}_{12}:\text{Er}^{3+}/0.22\text{Yb}^{3+}@\text{BiOF}:\text{Tm}^{3+}/\text{Yb}^{3+}$ composites are boosted, namely, the maximum S_a and S_r values are enhanced by around 2.48-fold and 1.38-fold, respectively, suggesting that the utilization of negative and positive thermal expansion combined luminescent materials is a facile and efficient technique to improve the thermometric properties of rare-earth ions. Furthermore, it is evident that not only is the S_a value of the developed composite much higher than those of other

reported rare-earth ion based optical thermometers, but also its S_r value is comparable with other previously developed optical thermometers (see Table 1). Besides, the reversibility of the developed composites is also explored so as to further reveal their feasibility for practical applications. The temperature-triggered switching of the FIR values of the $\text{Y}_2\text{Mo}_3\text{O}_{12}:\text{Er}^{3+}/0.22\text{Yb}^{3+}@\text{BiOF}:\text{Tm}^{3+}/\text{Yb}^{3+}$ composites was investigated, as shown in Fig. S10 (ESI†). Clearly, the FIR values are reversible and repeatable after several cycling heating–cooling processes. To better understand the reversibility of the developed composites, the repeatability (*i.e.*, R) is estimated *via* the function of $R = 1 - (\max|\bar{Q} - Q_i|)/\bar{Q}$ (where Q_i and \bar{Q} refer to the calculated FIR value and its average value, respectively) and its value is found to be as high as 94.5%.⁴³ In addition, with the aid of the following functions, the temperature uncertainty (*i.e.*, ΔT) of the thermometer *via* using the developed composites is detected, as defined:^{44,45}

$$\Delta T = \frac{1}{S_r} \frac{\delta \text{FIR}}{\text{FIR}} \quad (8)$$

$$\frac{\delta \text{FIR}}{\text{FIR}} = \sqrt{\left(\frac{\delta I_1}{I_1}\right)^2 + \left(\frac{\delta I_2}{I_2}\right)^2} \quad (9)$$

where I_1 and I_2 refer to the emission intensities of Tm^{3+} (blue) and Er^{3+} (green) ions, respectively, and δI_1 and δI_2 stand for the errors of I_1 and I_2 , respectively. Consequently, the ΔT value of the prepared composites is found to be 0.02–0.82 K when the temperature is changed in the range of 303–583 K. These results suggest that the $\text{Y}_2\text{Mo}_3\text{O}_{12}:\text{Er}^{3+}/0.22\text{Yb}^{3+}@\text{BiOF}:\text{Tm}^{3+}/\text{Yb}^{3+}$ composites with good reversibility, high sensitivities and wide operation temperature range are suitable for optical thermometry as temperature sensing luminescent materials.

4. Conclusion

In summary, a facile sol–gel reaction technique is adopted to prepare $\text{Y}_2\text{Mo}_3\text{O}_{12}:\text{Er}^{3+}/2x\text{Yb}^{3+}$ microparticles. Upon 980 nm excitation, the synthesized samples emit bright UC emission from the Er^{3+} ions and the optimal doping content for the Yb^{3+} ions in the $\text{Y}_2\text{Mo}_3\text{O}_{12}$ host lattice is 13 mol%. Owing to the NTE effect, anomalous thermal UC luminescence behaviors are observed in the $\text{Er}^{3+}/\text{Yb}^{3+}$ -codoped $\text{Y}_2\text{Mo}_3\text{O}_{12}$ microparticles. Through analyzing the temperature-dependent emission of TCLs, the thermometric performances of the $\text{Y}_2\text{Mo}_3\text{O}_{12}:\text{Er}^{3+}/0.22\text{Yb}^{3+}$ microparticles are estimated, in which the maximum S_a and S_r values are 6.79% K^{-1} and 0.79% K^{-1} , respectively. For the purpose of further improving the temperature sensing ability of the luminescent materials, we constructed $\text{Y}_2\text{Mo}_3\text{O}_{12}:\text{Er}^{3+}/0.22\text{Yb}^{3+}@\text{BiOF}:\text{Tm}^{3+}/\text{Yb}^{3+}$ composites. Since the UC emission intensities of Tm^{3+} and Er^{3+} ions display opposite temperature dependence, the developed composites possess splendid thermometric properties with high S_a and S_r values of 16.89% K^{-1} and 1.09% K^{-1} , respectively. These results demonstrate that the $\text{Er}^{3+}/\text{Yb}^{3+}$ -codoped $\text{Y}_2\text{Mo}_3\text{O}_{12}$ microparticles are potential candidates for optical thermometry and their



thermometric properties are able to be boosted *via* combination with a positive thermal expansion upconversion material.

Conflicts of interest

There are no conflicts to declare.

Acknowledgements

This work was supported by the K. C. Wong Magna Fund in Ningbo University (xkzw 1507), Natural Science Foundation of Zhejiang Province (LQ20F050004) and Key Research and Development Plan of Zhejiang Province (2019C04009).

Notes and references

- J. Xu, R. Shi, G. Chen, S. Dong, P. Yang, Z. Zhang, N. Niu, S. Gai, F. He, Y. Fu and J. Lin, *ACS Nano*, 2020, **14**, 9613–9625.
- X. Li, D. Chen, F. Huang, G. Chang, J. Zhao, X. Qiao, X. Xu, J. Du and M. Yin, *Laser Photonics Rev.*, 2018, **12**, 1800030.
- H. Suo, X. Zhao, Z. Zhang and C. Guo, *Chem. Eng. J.*, 2020, **389**, 124506.
- L. Luo, W. Ran, P. Du, W. Li and D. Wang, *Adv. Mater. Interfaces*, 2020, **7**, 1902208.
- S. Wang, J. Lin, Y. He, J. Chen, C. Yang, F. Huang and D. Chen, *Chem. Eng. J.*, 2020, **394**, 124889.
- Y. Liu, G. Bai, Y. Lyu, Y. Hua, R. Ye, J. Zhang, L. Chen, S. Xu and J. Hao, *ACS Nano*, 2020, **14**, 16003–16012.
- X. Wang, Y. Wang, L. Jin, Y. Bu, X. L. Yang and X. Yan, *J. Alloys Compd.*, 2019, **773**, 393–400.
- G. Xiang, X. Liu, Q. Xia, S. Jiang, X. Zhou, L. Li, Y. Jin, L. Ma, X. Wang and J. Zhang, *Inorg. Chem.*, 2020, **59**, 11054–11060.
- K. Trejgis, A. Bednarkiewicz and L. Marciniak, *Nanoscale*, 2020, **12**, 4667–4675.
- A. S. Lai, D. A. Hora, M. V. S. Rezende, Y. Xing, J. J. R. Jr, G. S. Maciel and M. A. R. C. Alencar, *Chem. Eng. J.*, 2020, **399**, 125742.
- P. Du, Y. Hou, W. Li and L. Luo, *Dalton Trans.*, 2020, **49**, 10224–10231.
- B. Cao, Y. Bao, Y. Liu, J. Shang, Z. Zhang, Y. He, Z. Feng and B. Dong, *Chem. Eng. J.*, 2020, **385**, 123906.
- G. Chen, R. Lei, F. Huang, H. Wang, S. Zhao and S. Xu, *Opt. Commun.*, 2018, **407**, 57–62.
- Y. Oba, T. Tadano, R. Akashi and S. Tsuneyuki, *Phys. Rev. Mater.*, 2019, **3**, 033601.
- K. Takenaka, *Front. Chem.*, 2018, **6**, 267.
- A. C. T. Dias, C. L. Lima, W. Paraguassu, K. P. Silva, P. T. C. Freire, J. M. Filhoa, B. A. Marinkovic, K. J. Miller, M. A. White and A. G. S. Filho, *Vib. Spectrosc.*, 2013, **68**, 251–256.
- X. Liu, B. Yuan, Y. Cheng, E. Liang and W. Zhang, *J. Alloys Compd.*, 2019, **776**, 236–241.
- C. Zhou, Q. Zhang, S. Liu, B. Luo, E. Yi, E. Tian, G. Li, L. Li and G. Wu, *Phys. Chem. Chem. Phys.*, 2017, **19**, 11778–11785.
- X. Liu, Y. Cheng, E. Liang and M. Chao, *Phys. Chem. Chem. Phys.*, 2014, **16**, 12848–12857.
- H. Zou, X. Yang, B. Chen, Y. Du, B. Ren, X. Sun, X. Qiao, Q. Zhang and F. Wang, *Angew. Chem., Int. Ed.*, 2019, **58**, 17255–17259.
- H. Zou, B. Chen, Y. Hu, Q. Zhang, X. Wang and F. Wang, *J. Phys. Chem. Lett.*, 2020, **11**, 3020–3024.
- J. Guo, B. Zhou, C. Yang, Q. Dai and L. Kong, *Adv. Funct. Mater.*, 2019, **29**, 1902898.
- C. Bradac, S. F. Lim, H. Chang and I. Aharonovich, *Adv. Opt. Mater.*, 2020, **8**, 2000183.
- Y. Li, Z. Cheng, L. Yao, S. Yang and Y. Zhang, *ACS Sustainable Chem. Eng.*, 2019, **7**, 18185–18196.
- J. Zhang and F. Qian, *Dalton Trans.*, 2020, **49**, 10949–10957.
- J. Qin, J. Xiang, H. Suo, Y. Chen, Z. Zhang, X. Zhao, Y. Wu and C. Guo, *J. Mater. Chem. C*, 2019, **7**, 11903–11910.
- B. A. Marinkovic, M. Ari, R. R. Avillez, F. Rizzo, F. F. Ferreira, K. J. Miller, M. B. Johnson and M. A. White, *Chem. Mater.*, 2009, **21**, 2886–2894.
- J. Hao, Y. Zhang and X. Wei, *Angew. Chem., Int. Ed.*, 2011, **50**, 6876–6880.
- M. Sójka, J. F. C. B. Ramalho, C. D. S. Brites, K. Fiaczyk, L. D. Carlos and E. Zych, *Adv. Opt. Mater.*, 2019, **7**, 1901102.
- M. Runowski, N. Stopikowska, D. Szeremeta, S. Goderski, M. Skwierczyńska and S. Lis, *ACS Appl. Mater. Interfaces*, 2019, **11**, 13389–13396.
- Y. Tong, W. Zhang, R. Wei, L. Chen and H. Guo, *Ceram. Int.*, 2021, **47**, 2600–2606.
- B. Hou, M. Jia, P. Li, G. Liu, Z. Sun and Z. Fu, *Inorg. Chem.*, 2019, **58**, 7939–7946.
- Q. Qiang, S. Du, X. Ma, W. Chen, G. Zhang and Y. Wang, *Dalton Trans.*, 2018, **47**, 8656–8662.
- T. Hu, Y. Gao, M. Molokeev, Z. Xia and Q. Zhang, *Sci. China Mater.*, 2019, **62**, 1807–1814.
- C. Wang, Y. Jin, L. Yuan, H. Wu, G. Ju, Z. Lia, D. Liu, Y. Lv, L. Chen and Y. Hu, *Chem. Eng. J.*, 2019, **374**, 992–1004.
- P. Du, J. Tang, W. Li and L. Luo, *Chem. Eng. J.*, 2021, **406**, 127165.
- R. Shi, L. Ning, Y. Huang, Y. Tao, L. Zheng, Z. Li and H. Liang, *ACS Appl. Mater. Interfaces*, 2019, **11**, 9691–9695.
- L. Li, X. Tang, Z. Wu, Y. Zheng, S. Jiang, X. Tang, G. Xiang and X. Zhou, *J. Alloys Compd.*, 2019, **780**, 266–275.
- D. Chen, L. Zhang, Y. Liang, W. Wang, S. Yan, J. Bi and K. Sun, *CrystEngComm*, 2020, **22**, 4438–4448.
- J. Xue, Z. Yu, H. M. Noh, B. R. Lee, B. C. Choi, S. H. Park, J. H. Jeong, P. Du and M. Song, *Chem. Eng. J.*, 2021, **415**, 128977.
- Y. Tong, W. Zhang, R. Wei, L. Chen and H. Guo, *Ceram. Int.*, 2021, **47**, 2600–2606.
- W. Zheng, B. Sun, Y. Li, T. Lei, R. Wang and Z. Wu, *ACS Sustainable Chem. Eng.*, 2020, **8**, 9578–9588.
- M. D. Dramićanin, *J. Appl. Phys.*, 2020, **128**, 040902.
- L. Zhou, P. Du and L. Li, *Sci. Rep.*, 2020, **10**, 20180.
- M. Sójka, J. F. C. B. Ramalho, C. D. S. Brites, K. Fiaczyk, L. D. Carlos and E. Zych, *Adv. Opt. Mater.*, 2019, **7**, 1901102.

